MNRAS 000, 1–8 (2020) Preprint 18 February 2022 Compiled using MNRAS LATEX style file v3.0

SDSS-IV MaNGA: Stellar population correlates with stellar root-mean-square velocity $V_{\rm rms}$ gradients or total-density-profile slopes at fixed effective velocity dispersion $\sigma_{\rm e}$

Shengdong Lu[1,2]★, Michele Cappellari[3], Shude Mao[4,1], Junqiang Ge[1], Ran Li[1,5]
[1]National Astronomical Observatories, Chinese Academy of Sciences, 20A Datun Road, Chaoyang District, Beijing 100101, China
[2]University of Chinese Academy of Sciences, Beijing 100049, China
[3]Sub-department of Astrophysics, Department of Physics, University of Oxford, Denys Wilkinson Building, Keble Road, Oxford, OX1 3RH, UK
[4]Department of Astronomy and Tsinghua Center for Astrophysics, Tsinghua University, Beijing 100084, China
[5]School of Astronomy and Space Science, University of Chinese Academy of Science, Beijing 100049, China

arXiv:2003.13625v3 [astro-ph.GA] 25 May 2020

Accepted ***. Received ***; in original form ***

ABSTRACT

Galaxy properties are known to correlate most tightly with the galaxy effective stellar velocity dispersion $\sigma_{\rm e}$. Here we look for *additional* trends at fixed $\sigma_{\rm e}$ using 1339 galaxies ($M_* \gtrsim 6\times10^9$ M$_\odot$) with different morphologies in the MaNGA (DR14) sample with integral-field spectroscopy data. We focus on the gradients ($\gamma_{\rm rms} \equiv \sigma(R_{\rm e}/4)/\sigma_{\rm e}$) of the stellar root-mean-square velocity ($V_{\rm rms} \equiv \sqrt{V^2+\sigma^2}$), which we show traces the total mass density gradient $\gamma_{\rm tot}$ derived from dynamical models and, more weakly, the bulge fraction. We confirm that $\gamma_{\rm rms}$ increases with $\sigma_{\rm e}$, age and metallicity. We additionally find that these correlations still exist at fixed $\sigma_{\rm e}$, where galaxies with larger $\gamma_{\rm rms}$ are found to be older and more metal-rich. It means that mass density gradients contain information of the stellar population which is not fully accounted for by $\sigma_{\rm e}$. This result puts an extra constraint on our understanding of galaxy quenching. We compare our results with galaxies in the IllustrisTNG hydrodynamical simulations and find that, at fixed $\sigma_{\rm e}$, similar trends exist with age, the bulge fraction, and the total mass density slope but, unlike observations, no correlation with metallicity can be detected in the simulations.

Key words: galaxies: formation – galaxy: evolution – galaxy: kinematics and dynamics – galaxies: structure

1 INTRODUCTION

Galaxy properties have already been found to strongly correlate with their morphologies. One of the quantities that are used to describe the morphology of galaxies is the bulge fraction. However, the photometric bulge-disk decomposition is a complex process, which depends on the extraction details and suffers from degeneracies (Cappellari et al. 2013b, hereafter C13b). Due to the degeneracies of projection, the intrinsic 3D stellar density cannot be uniquely recovered from the 2D images unless the galaxies are edge-on, even if we assume galaxies are axisymmetric (Rybicki 1987; Gerhard & Binney 1996; van den Bosch 1997; Magorrian et al. 1998). The fact that one cannot infer the intrinsic density of inclined galaxies implies that one cannot uniquely decompose their bulges and disks of inclined galaxies ($i < 90°$) unless we know the galaxies to be accurately described by Sersic (1968) bulges and exponential disks (Freeman 1970). Cappellari et al. (2011) used the *kinematic morphology* (i.e. fast and slow rotators) to study the relation between galaxy type and the environment density (i.e. the $T-\Sigma$ relation), instead of using classic morphology (i.e. lenticulars and ellipticals). It is found that the $T-\Sigma$ relation is cleaner when the kinematic morphology is adopted. It implies that combining dynamical properties may be beneficial for analyzing the structure of galaxies. In C13b, $\sigma_{\rm e}$ (the velocity dispersion within the half-light radius $R_{\rm e}$) is shown to be related to the bulge fraction of galaxies (see fig. 5 of C13b).

Cappellari et al. (2006) found that the stellar mass-to-light ratio M_*/L, which is related to the stellar population, tightly correlates with $\sigma_{\rm e}$ rather than mass or $R_{\rm e}$. Similarly, Graves et al. (2009) used the Fundamental Plane to conclude that no stellar population property shows any dependence on $R_{\rm e}$ at fixed $\sigma_{\rm e}$. The primary role of $\sigma_{\rm e}$ in driving variations in both the stellar population indicators (M_*/L, colors, and line indices) and the molecular gas content was clearly demonstrated by C13b and with population models by McDermid et al. (2015) using the high-quality data from the ATLAS$^{\rm 3D}$ survey. The latter ATLAS$^{\rm 3D}$ works showed that all population and gas content indicators closely follow lines of constant $\sigma_{\rm e}$ on the mass-size plane. It indicates that $\sigma_{\rm e}$, which traces

★ E-mail: lushengdong@nao.cas.cn

© 2020 The Authors

the bulge fraction, is the main driver for the observed trends of the stellar population properties on the mass-size plane. This result is verified with a larger sample of galaxies with different morphologies from SAMI (Scott et al. 2017, 1319 galaxies) and MaNGA (Li et al. 2018, ~ 2000 galaxies).

Given that galaxy properties correlate with σ_e and that this in turn appears related to the galaxies bulge fraction, or the steepness of the total density profile, it is natural to ask whether other quantities contain extra information on the population that is not already contained in σ_e alone. More specifically, we want to see whether there is a residual correlation of stellar population properties with the root-mean-aquare velocity ($V_{rms} \equiv \sqrt{V^2 + \sigma^2}$, where V and σ are the mean line-of-sight velocity and dispersion) profile at fixed σ_e. In C13b, the shape of V_{rms} map is proved to have the ability to trace the bulge fraction at even low inclinations (close to face-on, $i \sim 30°$, see fig. 4 of C13b). The gradient of V_{rms} (defined there as $\sigma(R_e/8)/\sigma_e$, where $\sigma(R_e/8)$ is the velocity dispersion within $R_e/8$), which encodes key information of the shape of the V_{rms} map (see Fig. 1 for some examples of the V_{rms} maps of MaNGA galaxies), is found to have similar distribution as stellar population properties on the mass-size plane, which implies the correlations between the gradient of V_{rms} and stellar populations. Notice that both σ_e, $\sigma(R_e/8)$, and $\sigma(R_e/4)$ in later text (see Eq. 2) are all luminosity-weighted V_{rms}, not purely dispersion σ in given apertures (see Eq. 3 for definition). However the ATLAS^{3D} sample only contains 260 galaxies and does not allow one to asses whether a residual trends exists at fixed σ_e, due to the small-numbers statistics (see Cappellari 2016 for a review).

With the advancement of the largest Integral Field Unit (IFU) survey MaNGA (Bundy et al. 2015), we are able to study the underlying relations between the kinematics and the stellar populations in detail with a sufficiently large number of galaxies with different morphologies. The goals of this paper are: **(i)** to investigate the correlations between the gradient of V_{rms} and galaxy properties (i.e. age, metallicity, the bulge fraction, and the steepness of total mass profile); **(ii)** to examine whether the correlations still exist at fixed σ_e which has not been addressed before; **(iii)** to compare with the state-of-the-art hydrodynamical simulations, the IllustrisTNG simulations (Marinacci et al. 2018; Naiman et al. 2018; Nelson et al. 2018; Pillepich et al. 2018; Springel et al. 2018).

This paper is organized as follows. In Section 2, we describe our sample selection in MaNGA (Section 2.1) and IllustrisTNG simulations (Section 2.2). The general property of the V_{rms} gradient is presented in Section 3.1. Section 3.2 is devoted to presenting the correlations between the gradient of V_{rms} and galaxy properties. In Section 3.3, we investigate the relations between the gradient of V_{rms} and galaxy properties at fixed σ_e. Finally, we summarize our findings in Section 4.

2 DATA

2.1 MaNGA galaxies

The galaxies in this study are from the MaNGA sample released by SDSS DR14 (Abolfathi et al. 2018), which includes 2778 galaxies with different morphologies. We note here that we do not use the latest data release of MaNGA because we want our results to rely on published data (i.e. stellar population and structural properties) from other papers. The kinematical data are extracted from the IFU spectra using the MaNGA data analysis pipeline (DAP; Westfall et al. 2019) by fitting absorption lines, making use of the PPXF software (Cappellari & Emsellem 2004; Cappellari 2017) with a subset of the MILES (Sánchez-Blázquez et al. 2006; Falcón-Barroso et al. 2011) stellar library, MILES-THIN. Before fitting, the spectra are Voronoi binned (Cappellari & Copin 2003) to S/N = 10. Readers are referred to the following papers for more details on the MaNGA instrumentation (Drory et al. 2015), observing strategy (Law et al. 2015), spectrophotometric calibration (Smee et al. 2013; Yan et al. 2016a), and survey execution and initial data quality (Yan et al. 2016b).

We exclude the galaxies which are merging or have low data quality (with fewer than 100 Voronoi bins with S/N greater than 10) from our sample. Besides, we exclude galaxies with low stellar mass ($M_* < 6 \times 10^9\,M_\odot$) to achieve a comparable minimum stellar mass as in C13b. The stellar mass of MaNGA galaxies is derived from Salim et al. (2016, table 1), in which the state-of-the-art spectral energy distribution (SED) fitting of UV and optical fluxes is adopted. After excluding the galaxies described above, we have 1520 galaxies with different morphologies. We derive the stellar population properties (i.e. age and metallicity) from Li et al. (2018, see their online table A1), which are calculated as the luminosity-weighted values within an elliptical aperture of area $A = \pi R_e^2$. We use the mass-weighted total density slope (γ_{tot}) from Li et al. (2019, a subset[1] of the values for our galaxies is included in Table 1) to describe the total mass profiles of galaxies (see Li et al. 2019, eq. 2 for definition). The bulge-to-total luminosity ratio (B/T) is from Simard et al. (2011, table 1). After cross-matching these four catalogs, we have 1339 galaxies with available galaxy properties in our final sample. The size parameters (i.e. the half-light radius R_e and the major axis of the half-light isophote R_e^{maj}) used in this work are calculated from the Multi-Gaussian Expansion (MGE) models (Emsellem et al. 1994) with the fitting algorithm and PYTHON software[2] by Cappellari (2002) and are scaled by a factor of 1.35 (see fig. 7 of Cappellari et al. 2013a).

2.2 Galaxies in hydrodynamical simulations

For comparison, we also select a sample of simulated galaxies with the same stellar mass range ($M_* > 6 \times 10^9\,M_\odot$) at $z = 0$ from the state-of-the-art magneto-hydrodynamic cosmological galaxy formation simulations, the IllustrisTNG simulations[3] (TNG hereafter; Marinacci et al. 2018; Naiman et al. 2018; Nelson et al. 2018; Pillepich et al. 2018; Springel et al. 2018). In this work, we use its full-physics version with a cubic box of 110.7 kpc side length (TNG100) which has been made publicly available (Nelson et al. 2019). The mass resolutions of the TNG100-full physics version for baryonic and dark matter are $m_{baryon} = 1.4 \times 10^6\,M_\odot$ and $m_{DM} = 7.5 \times 10^6\,M_\odot$, with a gravitational softening length of $\epsilon = 0.74$ kpc. Gas cells are resolved in a fully adaptive manner with a minimum softening length of 0.19 comoving kpc. All selected galaxies are central galaxies whose host dark matter subhaloes are identified by the SUBFIND algorithm (Springel et al. 2001; Dolag et al. 2009). Thus, we have 5105 simulated galaxies in our sample.

To derive stellar population properties of simulated galaxies, we first project them along the X-axis of the simulation box to produce mock images in the SDSS r-band (Stoughton et al. 2002) fil-

[1] Readers need to cite Li et al. (2019) if they want to use the total density slope in this work.
[2] The software is available from http://www-astro.physics.ox.ac.uk/~mxc/software
[3] http://www.tng-project.org

ter. We then use the MGE method to obtain their size parameters as for real galaxies. The age and metallicity of TNG galaxies are calculated as luminosity-weighted log Age and [Z/H] within an elliptical aperture of area $A = \pi R_{\rm e}^2$ using the equation below:

$$\langle x \rangle = \frac{\Sigma_k L_k x_k}{\Sigma_k L_k}, \quad (1)$$

where x_k is log Age (or [Z/H]) of the k-th particle within this elliptical aperture, and L_k is the SDSS r-band luminosity of the k-th particle. The bulge-to-total ratio of TNG galaxies is from Xu et al. (2019). We refer the readers to Xu et al. (2017) for detailed descriptions of galaxy property extraction. The total mass density slopes of TNG galaxies are from Li et al. (2019). All these related properties of TNG galaxies can be derived from the journal website and readers are required to cite Xu et al. (2019) if they need to use the bulge fraction in this work.

We note here that we want to make an impeccable comparison with the IllustrisTNG simulations, and as a result, we exclude the galaxies with low stellar mass ($M_* < 6\times10^9\,{\rm M}_\odot$) in MaNGA. This mass limit roughly matches the mass cutoff of the IllustrisTNG simulations ($\sim 5\times10^9\,{\rm M}_\odot$, below which the galaxies may not be sufficiently resolved). We have also examined our results with all qualified galaxies in MaNGA regardless of their stellar masses and find our results remain unchanged.

3 RESULTS

In this section, we first present the distribution of the gradient of $V_{\rm rms}$ in Section 3.1. Then we show the relations between the gradient of $V_{\rm rms}$ and galaxy properties (i.e. B/T, $\gamma_{\rm tot}$, log Age, and [Z/H]) in Section 3.2. Section 3.3 is devoted to presenting the relation between the gradient of $V_{\rm rms}$ and galaxy properties at fixed $\sigma_{\rm e}$.

3.1 The gradient of $V_{\rm rms}$

Similarly to C13b, we define the gradient of $V_{\rm rms}$ as:

$$\gamma_{\rm rms} \equiv \frac{\sigma(R_{\rm e}/4)}{\sigma_{\rm e}}. \quad (2)$$

$\sigma_{\rm e}$ is the luminosity-weighted $V_{\rm rms}$ within an elliptical aperture of area $A = \pi R_{\rm e}^2$ and is calculated as:

$$\sigma_{\rm e} = \sqrt{\frac{\Sigma_k F_k V_{{\rm rms},k}^2}{\Sigma_k F_k}} = \sqrt{\frac{\Sigma_k F_k (V_k^2 + \sigma_k^2)}{\Sigma_k F_k}}, \quad (3)$$

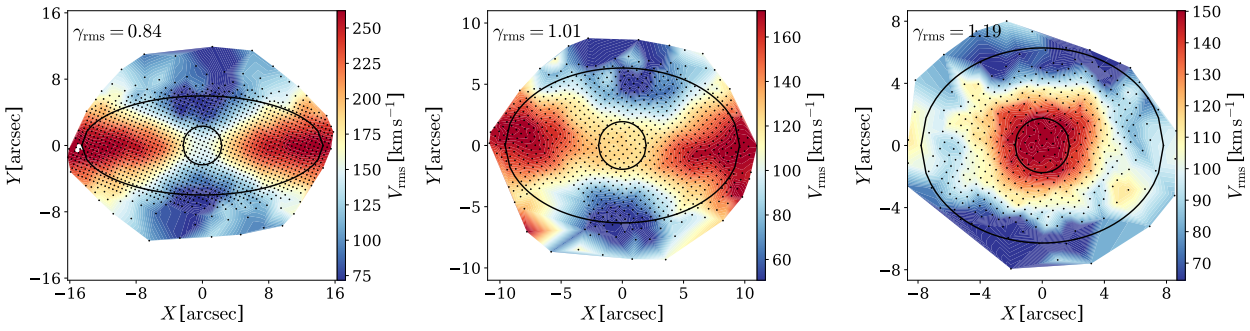
where V_k and σ_k are the mean velocity and dispersion in the k-th IFU spaxel, and F_k is the flux in the k-th spaxel. The sum is within the elliptical aperture described above. $\sigma(R_{\rm e}/4)$ is calculated in the same way but the sum is within a *circular* aperture with radius of $R_{\rm e}/4$ (see Fig. 1 for examples). The $\sigma(R_{\rm e}/4)$ and $\sigma_{\rm e}$ so defined agree closely with the velocity dispersions measured from a single fit to the spectrum inside the same apertures in C13b (Li et al. 2018). If a galaxy has $\gamma_{\rm rms} > 1$, that means there is a decrease of $V_{\rm rms}$ from the inner to the outer region of this galaxy. We note here that due to the limitation of spatial resolution in MaNGA, we use a larger ($R_{\rm e}/4$ instead of $R_{\rm e}/8$) aperture for the central velocity dispersion compared to that in C13b. We show some examples of the $V_{\rm rms}$ maps of MaNGA galaxies in Fig. 1, from which we can see an obvious change of the map shape from low $\gamma_{\rm rms}$ to high $\gamma_{\rm rms}$ (see Section 3.2 for more detailed discussion). Part of the quantitative results are listed in Table 1. For simulated galaxies, $\langle v_{\rm los}^2 \rangle^{1/2}$ is used to approximate the $V_{\rm rms}$.

Due to the effect of seeing, we have tried to only use galaxies with $R_{\rm e}/4 > 1.5''$, where $1.5''$ is the typical value of seeing in MaNGA (see Bundy et al. 2015 for more information of technical details of MaNGA), which constitute about half of our current sample (red circles with green dots in the center in Fig. 3 and Fig. 4). Our main results are found to be unchanged with only large galaxies. Besides, we have also tried to use the linear slopes of log $V_{\rm rms}$ profiles (log $V_{\rm rms}$ versus log R) to describe the gradient of $V_{\rm rms}$. We first divide the galaxies into several elliptical annuli from $R_{\rm e}/8$ to $R_{\rm e}$, with the global ellipticity measured around $1R_{\rm e}$. Then we calculate the median value of log $V_{\rm rms}$ in each annulus and perform a linear fit to get the linear slopes. We find that our main results remain unchanged when the new gradient is adopted.

We show the distribution of $\gamma_{\rm rms}$ ($\equiv \sigma(R_{\rm e}/4)/\sigma_{\rm e}$) on the $R_{\rm e}^{\rm maj}$-$M_{1/2}$ plane (the 'mass-size plane') in Fig. 2, where $M_{1/2}$ is the enclosed total mass within a spherical aperture of the three-dimensional half-light radius. The $M_{1/2}$ here is from Li et al. (2018) which is derived using the Jeans anisotropic model (JAM) (Cappellari 2008). Before plotting, we make use of the PYTHON implementation[4] (see details in C13b) of the two-dimensional Locally Weighted Regression (LOESS) (Cleveland & Devlin 1988) method to obtain smoothed distribution of $\gamma_{\rm rms}$. As can be seen, the gradient of $V_{\rm rms}$ varies systematically roughly along the $\sigma_{\rm e}$ direction, which is consistent with the result in C13b (the top panel of their fig. 6) in which $\sigma(R_{\rm e}/8)/\sigma_{\rm e}$ is used. We note here that due to the fact that we use a different definition of the gradient of $V_{\rm rms}$ from C13b and our samples include late-type galaxies which typically have lower $\gamma_{\rm rms}$, the smoothed $\gamma_{\rm rms}$ values obtained with the LOESS method in this figure are somehow lower than those in C13b.

To better illustrate the correlation between $\gamma_{\rm rms}$ and $\sigma_{\rm e}$, we present Fig. 3. As shown in the figure, $\gamma_{\rm rms}$ of MaNGA galaxies increases with $\sigma_{\rm e}$ from $\gamma_{\rm rms} < 1$ (at low $\sigma_{\rm e}$) to $\gamma_{\rm rms} > 1$ (at high $\sigma_{\rm e}$). The transition point $\gamma_{\rm rms} = 1$, which corresponds to a flat $V_{\rm rms}$ profile, is at $\log\sigma_{\rm e} \approx 2.1$. For $\log\sigma_{\rm e} \gtrsim 2.1$, the trend becomes flatter and $\gamma_{\rm rms}$ stays at ~ 1.05, indicating a mild decrease of $V_{\rm rms}$ from the central region of galaxies to the outer part. As demonstrated in C13b (fig. 5), galaxies with $\log\sigma_{\rm e} \approx 2.0$ have $V_{\rm rms}$ maps in butterfly-like shapes with small bulges in the center, after which the peak of $V_{\rm rms}$ in the center gets stronger, indicating a rising bulge fraction. It implies that the relation between the gradient of $V_{\rm rms}$ and the bulge fraction saturates when this is larger than a threshold. In the idealized case in which the bulge and disk have fixed parametrization (e.g. exponential and Sérsic profiles), this can be qualitatively understood as due to the fact that, when the bulge dominates, the $V_{\rm rms}$ gradient must converge to that of the bulge alone. The most massive galaxies ($M_* > 2\times10^{11}\,{\rm M}_\odot$), which also have large $\sigma_{\rm e}$, tend to be slow rotators without disks. For those galaxies, $V \sim 0$ and the $V_{\rm rms}$ coincides with the σ, which has a characteristic decreasing radial profile with radius. This is illustrated in Fig. 4, in which $\gamma_{\rm rms}$ increases with B/T and levels off when B/T $\gtrsim 0.5$ (see Section 3.2 for a detailed description). This trend in $\gamma_{\rm rms}$ with $\sigma_{\rm e}$ is similar with the trend in total density slope $\gamma_{\rm tot}$ found by Poci et al. (2017) and Li et al. (2019), which also shows a near constant trend above $\log\sigma_{\rm e} \approx 2.1$ and a break, and

[4] The software is available from https://pypi.org/project/loess/



(a) 1-211082 (b) 1-114145 (c) 1-48208

Figure 1. Three examples (MaNGA ID: 1-211082, 1-114145, 1-48208) of the $V_{\rm rms}$ ($\equiv \sqrt{V^2 + \sigma^2}$) maps of MaNGA galaxies with different $\gamma_{\rm rms}$. In each panel, the outer ellipse encloses an area $A = \pi R_{\rm e}^2$, while the inner circular has radius $R_{\rm e}/4$.

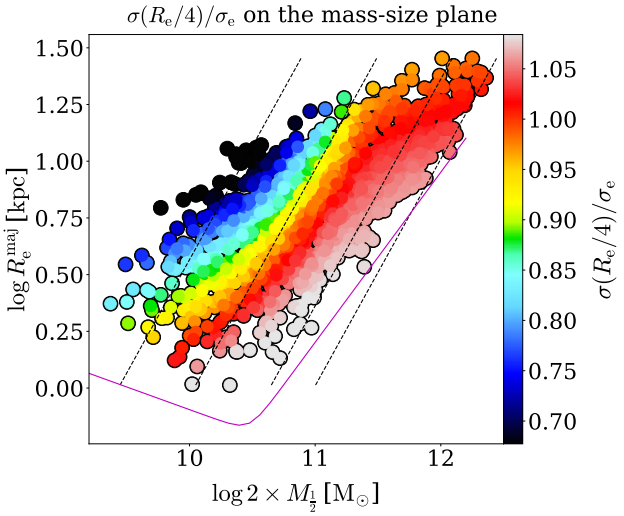


Figure 2. The distribution of MaNGA galaxies on the mass-size plane ($R_{\rm e}^{\rm maj}$ vs. $M_{1/2}$), color-coded by the $V_{\rm rms}$ gradient $\gamma_{\rm rms}$ ($\equiv \sigma(R_{\rm e}/4)/\sigma_{\rm e}$). The black dashed lines are the lines of constant $\sigma_{\rm e}$: 50, 100, 200, and 300 km s^{-1}. The magenta curve is the zone of exclusion defined in C13b.

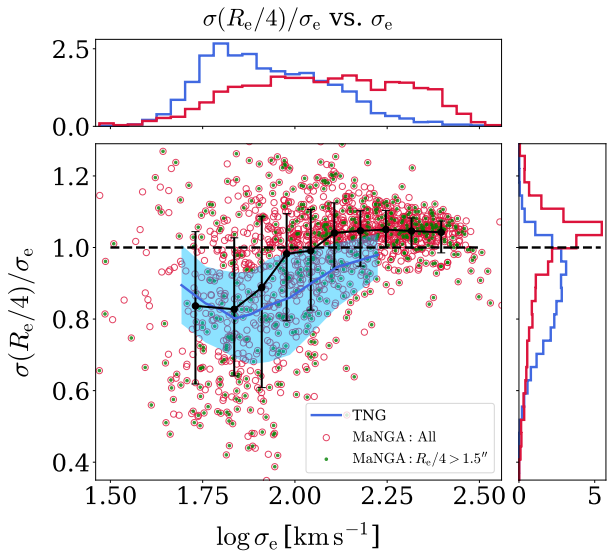


Figure 3. The relation between the $V_{\rm rms}$ gradient $\gamma_{\rm rms}$ and $\sigma_{\rm e}$. The red circles are MaNGA galaxies and the circles with green dots in the center are the galaxies with $R_{\rm e}/4 > 1.5''$, where $1.5''$ is the typical value of seeing in MaNGA. The black dots represent the median values of $\gamma_{\rm rms}$ in each $V_{\rm rms}$ bin, with error bars indicating the 1σ range. TNG galaxies are shown by the median profile (blue lines) with a shaded region indicating the 1σ range. The black dashed line represents $\gamma_{\rm rms} = 1$, below which an increase of $V_{\rm rms}$ exists in galaxies. The histograms are the distributions of $\gamma_{\rm rms}$ and log $\sigma_{\rm e}$ for MaNGA (red) and TNG (blue) galaxies.

an increase in $\gamma_{\rm tot}$, below that transition value (see fig.1 of Li et al. 2019). The key difference is that $\gamma_{\rm rms}$ is a purely empirical quantity, which does not involve dynamical models. As a comparison, however, TNG galaxies show a decreasing trend at low $\sigma_{\rm e}$ end and do not show a flat tail at high $\sigma_{\rm e}$ end. Besides, most ($\sim 86\%$) TNG galaxies have $\gamma_{\rm rms} < 1$, relative to 44% in MaNGA, and $\sigma_{\rm e}$ of TNG galaxies is typically lower than MaNGA galaxies. This may be due to the overly-strong AGN feedback (typically the isotropic black hole kinetic winds in the AGN quiescent phase) in IllustrisTNG for puffing up the galaxies (Wang et al. 2019, 2020; Lu et al. 2020).

3.2 $\gamma_{\rm rms}$ vs. galaxy properties

To investigate the relation between the $V_{\rm rms}$ gradient and galaxy properties (i.e. the stellar age, metallicity, the total density slope, and the bulge fraction), we present Fig. 4. As can be seen, $\gamma_{\rm rms}$ of MaNGA galaxies increases with log Age and [Z/H], indicating that older and more metal-rich galaxies are more likely to have flatter or even declining $V_{\rm rms}$ profiles. For TNG galaxies, $\gamma_{\rm rms}$ shows a shallower correlation with log Age, while it does not show an obvious correlation with [Z/H]. We note here that TNG lacks galaxies with low metallicity which results in the narrower range of metallicity.

Regarding the galaxy structural parameters, one can note that $\gamma_{\rm rms}$ ($\equiv \sigma(R_{\rm e}/4)/\sigma_{\rm e}$) increases with bulge fraction until B/T $\sim$ 0.5, but flattens for larger B/T values. This implies that either $\gamma_{\rm rms}$ is not a good indicator of bulge fraction for nearly pure spheroids (see also Section 3.1), or that extreme bulge fractions are more difficult to measure from photometry. For the total density slope $\gamma_{\rm tot}$,

MaGNA ID	log $R_{\rm e}$ [arcsec]	log $R_{\rm e}^{\rm maj}$ [arcsec]	log $\sigma(R_{\rm e}/4)$ [km s^{-1}]	log $\sigma_{\rm e}$ [km s^{-1}]	$\gamma_{\rm rms}$	$\gamma_{\rm tot}$
1-24295	0.85	0.85	2.27	2.16	1.05	1.95
1-260743	0.78	0.79	2.44	2.42	1.01	2.06
1-115128	0.90	1.07	1.83	1.97	0.93	1.83
1-258820	1.11	1.25	1.09	1.87	0.59	1.14
1-251662	0.76	0.78	2.24	1.98	1.13	1.78
1-637825	1.05	1.14	1.53	1.92	0.80	1.62
1-23877	1.02	1.31	1.70	2.09	0.82	1.60
1-109521	0.85	0.91	2.32	2.28	1.02	2.02
1-321967	0.39	0.45	1.88	1.88	1.00	1.74
1-147685	0.88	1.28	0.82	1.95	0.42	0.73
1-547185	0.93	0.99	1.76	1.83	0.96	1.84
1-38550	1.15	1.21	1.82	1.84	0.99	1.53
1-351790	0.62	0.73	1.56	1.66	0.94	1.50
1-258315	0.85	0.89	1.75	1.87	0.94	1.71
1-95770	0.85	0.95	1.64	1.87	0.88	0.98
1-22347	0.46	0.49	2.00	1.98	1.01	1.89
1-135091	0.87	0.94	2.28	2.22	1.02	2.05
1-260541	0.89	0.90	2.63	2.39	1.10	2.10
1-93908	0.85	0.91	2.58	2.33	1.11	2.35
1-275354	0.93	1.04	1.56	1.81	0.86	1.57
1-339116	0.67	0.81	1.34	1.81	0.74	1.30
1-167392	0.51	0.64	1.25	1.79	0.70	0.49
1-174036	0.78	0.82	2.27	2.37	0.95	1.80
1-55552	0.76	0.81	2.44	2.27	1.07	2.18
1-24476	0.96	1.05	2.19	2.08	1.05	2.01
1-545674	1.27	1.43	1.38	1.75	0.79	0.64
1-251278	0.66	0.70	2.54	2.35	1.08	2.20
1-594505	0.93	0.93	2.40	2.23	1.08	2.37
1-167334	0.60	0.68	2.06	2.00	1.03	2.39
1-217557	0.53	0.58	2.22	2.08	1.07	2.52
1-245908	0.57	0.68	1.99	1.95	1.02	1.96
1-44047	0.32	0.42	1.98	2.11	0.94	1.80
1-210667	1.12	1.25	1.64	1.76	0.93	1.28
1-73638	0.87	1.04	2.06	2.28	0.90	1.88
1-256465	0.61	0.66	2.38	2.28	1.04	2.42
1-114171	0.73	0.79	2.60	2.45	1.06	2.26
1-210961	0.58	0.86	1.89	2.03	0.93	2.16
1-217650	0.82	0.85	1.92	1.89	1.02	1.94
1-166739	0.83	0.88	2.40	2.32	1.04	2.26
1-164007	0.47	0.60	2.05	2.04	1.01	1.90
1-245940	0.91	1.03	2.36	2.52	0.93	2.03
1-274506	0.86	0.93	0.84	1.65	0.51	0.50
1-156011	0.75	0.75	2.57	2.09	1.23	2.31
1-210116	1.18	1.23	1.93	1.94	1.00	1.72
1-180208	0.55	0.67	2.44	2.27	1.07	2.90
12-84674	0.99	1.00	1.77	1.72	1.03	1.41
1-96075	1.05	1.11	1.82	2.07	0.88	1.61
1-23786	0.84	0.98	1.06	1.81	0.59	0.87
1-36977	0.78	0.81	2.20	2.12	1.04	2.00
1-457009	0.87	0.91	1.91	1.79	1.07	1.44
1-43272	0.47	0.53	1.57	1.81	0.87	1.22
12-84627	0.82	1.01	1.51	2.05	0.74	1.76
1-29726	0.68	0.77	2.55	2.44	1.04	2.28
1-38398	1.00	1.30	1.53	1.95	0.79	1.48
1-492524	0.79	1.03	1.69	1.83	0.92	1.67
1-273861	0.41	0.42	2.20	2.11	1.04	2.25
1-384548	0.43	0.56	2.33	2.22	1.05	2.56

Table 1. MaNGA ID, half-light radius log $R_{\rm e}$, major axis of the half-light isophote log $R_{\rm e}^{\rm maj}$, luminosity-weighted velocity dispersion within two apertures (a circular aperture with radius $R_{\rm e}/4$ and an elliptical aperture of area $A = \pi R_{\rm e}^2$), the gradient of $V_{\rm rms}$ ($\gamma_{\rm rms} \equiv \sigma(R_{\rm e}/4)/\sigma_{\rm e}$), and the total density slope $\gamma_{\rm tot}$ (from Li et al. 2019) for part of our sample. Please see the complete table on the journal website.

which is defined as (Dutton & Treu 2014, eq. 1):

$$\gamma_{\rm tot} \equiv -\frac{1}{M\,(R_{\rm e})}\int_0^{R_{\rm e}} 4\pi r^2 \rho(r)\frac{d\log\rho}{d\log r}dr = 3 - \frac{4\pi R_{\rm e}^3 \rho\,(R_{\rm e})}{M\,(R_{\rm e})}, \quad (4)$$

where $\rho(r)$ is total mass density of the galaxy and $M(R)$ is the total mass enclosed in a sphere with radius R (Li et al. 2019), the gradient of $V_{\rm rms}$ rises across the whole range of $\gamma_{\rm tot}$. It means that the steeper the mass profile, the more likely the $V_{\rm rms}$ profile to be flat or even declining. $\gamma_{\rm rms}$ of galaxies which are isothermal ($\gamma_{\rm tot} = 2$) is ~ 1, indicating that flat $V_{\rm rms}$ profiles are exsitent in these galaxies. A purely isothermal spherical isotropic galaxy has constant $V_{\rm rms}$ (Binney & Tremaine 2008, denoted by σ in their eq. 4.100), while in this work, the same correspondence between $\gamma_{\rm tot} = 2$ and flat $V_{\rm rms}$ profile also works in our non-spherical case. By contrast, TNG galaxies show a gradually increasing but somehow shallower trend of $\gamma_{\rm rms}$ towards the high B/T and high $\gamma_{\rm tot}$ end.

3.3 Relations at fixed $\sigma_{\rm e}$

The results in Section 3.2 are generally consistent with the previous studies (Cappellari et al. 2013b; Scott et al. 2017; Li et al. 2018), in which stellar age, metallicity, and the gradient of $V_{\rm rms}$ are found to have similar distributions on the mass-size plane, indicating a correlation among them. However, it is still unclear whether the relations are only driven by $\sigma_{\rm e}$, or in other words, whether the gradient of $V_{\rm rms}$ still correlates with galaxy properties at fixed $\sigma_{\rm e}$.

To answer this question, we first divide galaxies in our sample into 10 bins according to their log $\sigma_{\rm e}$, with the same number of galaxies in each bin. Then galaxies in each bin are further divided into two subgroups according to their $V_{\rm rms}$ gradient $\gamma_{\rm rms}$ ($\gamma_{\rm rms} > \gamma_{\rm rms,50}$ and $\gamma_{\rm rms} < \gamma_{\rm rms,50}$, where $\gamma_{\rm rms,50}$ is the median value of $\gamma_{\rm rms}$ in each $V_{\rm rms}$ bin). Finally, we calculate the median values of galaxy properties for galaxies of both two subgroups in each bin.

Fig. 5 shows the trends of galaxy properties as a function of log $\sigma_{\rm e}$ for both subgroups ($\gamma_{\rm rms} > \gamma_{\rm rms,50}$ and $\gamma_{\rm rms} < \gamma_{\rm rms,50}$). It can be clearly seen that, although with large scatters, MaNGA galaxies with different $V_{\rm rms}$ gradients ($\gamma_{\rm rms}$) appear to show systematic differences between each other. At fixed $\sigma_{\rm e}$, galaxies with larger $\gamma_{\rm rms}$ (red lines) are typically older, more metal-rich, more bulge-dominated, and have steeper mass profiles.

To quantitatively describe the discrepancy between the two subgroups ($\gamma_{\rm rms} > \gamma_{\rm rms,50}$ and $\gamma_{\rm rms} < \gamma_{\rm rms,50}$), we employ a statistical analysis to estimate the probability of the difference being statistically significant. Thus, we set our null hypothesis H_0 to be: the two subgroups ($\gamma_{\rm rms} > \gamma_{\rm rms,50}$ and $\gamma_{\rm rms} < \gamma_{\rm rms,50}$) do not have systematic difference in age (or other parameters). In the i-th log $\sigma_{\rm e}$ bin, if the discrepancy we see for the two subgroups arises by chance, the age (or other investigated parameters) difference should follow a normal distribution with its mean value being 0 and its variance being the combination of the errors of the two subgroups:

$$\sigma_i^2 = \sigma_{i,\gamma_{\rm rms}>\gamma_{\rm rms,50}}^2 + \sigma_{i,\gamma_{\rm rms}<\gamma_{\rm rms,50}}^2, \quad (5)$$

where $\sigma_{i,\gamma_{\rm rms}>\gamma_{\rm rms,50}}$ and $\sigma_{i,\gamma_{\rm rms}<\gamma_{\rm rms,50}}$ are the standard deviations of age (or other parameters) of the two subgroups in i-th bin. We randomly sample from the 10 (the number of log $\sigma_{\rm e}$ bins) normal distributions, and define:

$$\Delta = \sum_{i=1}^{10} \frac{\delta_i}{\sigma_i}, \quad (6)$$

where δ_i is the value randomly sampled from the normal distribution of the i-th bin. Then we compare Δ with the observed relative

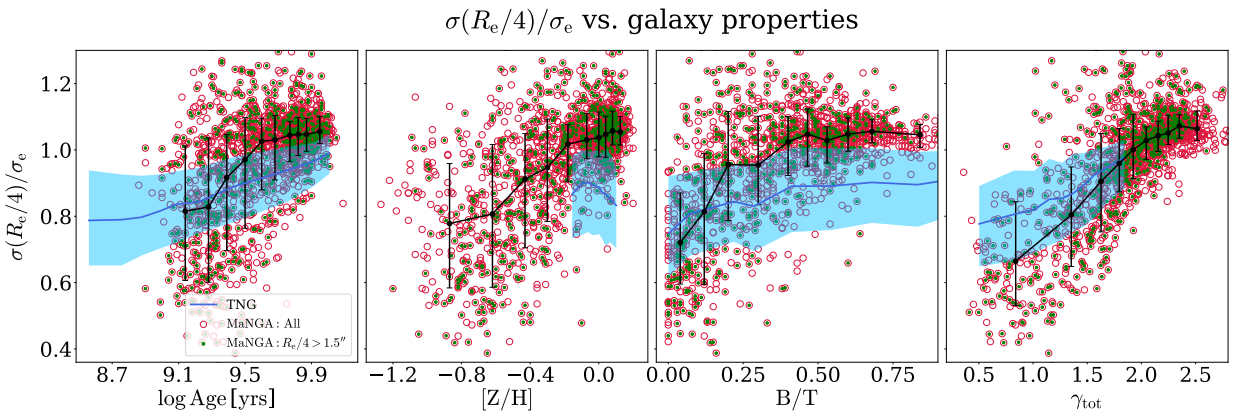


Figure 4. The relation of γ_{rms} vs. log Age, [Z/H], B/T, and the total density slope γ_{tot} (from left to right). The bulge fraction of MaNGA galaxies is derived from Simard et al. (2011, table 1). The symbols are the same as Fig. 3.

difference ($\Delta_{ob} \equiv \sum_{i=1}^{10} \delta_{ob,i}/\sigma_i$, where $\delta_{ob,i}$ is the difference we see in Fig. 5 of the two subgroups in the i-th bin). We want to evaluate the probability of seeing all sampled δ_iâĂŹs being positive and Δ greater than the observed value, Δ_{ob}, by random fluctuations.

To do this, we perform Monte Carlo samplings mentioned above by 4×10^6 times, and find that $P(\Delta > \Delta_{ob}, \delta_i > 0) \sim 0.09\%$ for galaxy age, metallicity and B/T, and $\sim 0.03\%$ for γ_{tot} (see Fig. 6 for the distributions of sampled values). Given such low probabilities of our observed differences arising by chance, we reject our null hypotheses and conclude that there is indeed systematic difference in both stellar population properties and structural parameters of galaxies with different γ_{rms} at fixed σ_e.

In comparison, the two subgroups of TNG galaxies also show discrepancies in the mass density slope, the bulge fraction, and the stellar age with $P(\Delta > \Delta_{ob}, \delta_i > 0)$ being $\sim 0.1\%$, $\sim 0.1\%$, and $\sim 0.09\%$, respectively. For metallicity, however, the difference between the two subgroups is again completely absent in the simulations. In particular, TNG galaxies span a rather limited range of [Z/H] compared to the observations, making any comparison with the observations flawed from the start.

The results seen from Fig. 5 indicate that the relations between σ_e and galaxy properties are not only driven by σ_e, but also by the gradient of V_{rms}. The fact that the gradient of V_{rms} contains information of both stellar populations and structural properties of galaxies, which are not fully accounted for by σ_e, has not been addressed before.

4 CONCLUSION AND DISCUSSION

In this work, we study the relations between the gradient of V_{rms} ($\equiv \sqrt{V^2 + \sigma^2}$) and galaxies properties (i.e. the mass-weighted total density slope γ_{tot}, the bulge fraction B/T, galaxy age log Age, and metallicity [Z/H]) with 1339 galaxies from the MaNGA sample released by SDSS DR14, and make a comparison with the hydrodynamical simulations, the IllustrisTNG (TNG) simulations.

We employ γ_{rms} ($\equiv \sigma(R_e/4)/\sigma_e$) to represent the gradient of V_{rms} and find that γ_{rms} changes systematically on the mass-size plane roughly along the direction of σ_e, consistent with C13b. Besides, γ_{rms} increases with $\log \sigma_e$ below $\log \sigma_e \approx 2.1$. At high σ_e end, the V_{rms} gradient keeps nearly unchanged at $\gamma_{rms} \approx 1.05$, indicating a saturation in the V_{rms} slope for bulge-dominated galaxies (B/T $\gtrsim 0.5$). Most galaxies ($\sim 86\%$) in TNG appear to have $\gamma_{rms} < 1$, which means a decreasing trend of V_{rms} from inner to outer regions in galaxies, relative to 44% in MaNGA. It may be due to the overly-strong AGN feedback in TNG (Wang et al. 2019, 2020; Lu et al. 2020).

We find that V_{rms} gradients γ_{rms} are closely related (in a non-linear way) to both the total mass density gradients γ_{tot} and, more weakly, to the bulge fraction B/T, which is a more uncertain quantity. We confirm the clear trends of γ_{rms} with σ_e, age and metallicity (e.g. fig. 22 in the review by Cappellari 2016). The correlation of γ_{rms} with age is more shallow in TNG than in the observations and our clear empirical correlation of γ_{rms} with [Z/H] is completely absent in TNG.

The main goal of this paper is to look for trends in galaxy properties at fixed σ_e, which were impossible to investigate from smaller samples than MaNGA. We found that at fixed σ_e the stellar population clearly depends on the density gradients as here quantified by γ_{rms}. In particular, at fixed σ_e, galaxies with larger γ_{rms} are still older and more metal-rich. It means that both stellar populations and structural properties of galaxies are not fully accounted for by σ_e and the gradient of V_{rms} also contains these information. In TNG, galaxy age, γ_{tot}, and B/T show qualitatively similar trends as we derive from the MaNGA data, but the trends at fixed σ_e of γ_{rms} with [Z/H], which are clearly visible in MaNGA, are again completely absent in the simulations. It implies that the relation between metallicity and stellar age (and also other galaxy properties) seen in observations is not met in TNG.

This new empirical evidence that galaxy properties still correlate with the V_{rms} gradient γ_{rms} at fixed σ_e provides an extra constraint on our understanding of galaxy quenching. In the current state-of-the-art simulations (e.g. the IllustrisTNG simulations), the relations between galaxy properties and γ_{rms} are not well recovered, which shows the power of investigating this extra quantity – it can be used to validate the simulations in terms of the relations between stellar population and dynamical properties of galaxies.

ACKNOWLEDGEMENTS

This work is partly supported by the National Key Basic Research and Development Program of China (No. 2018YFA0404501 to SM), by the National Natural Science Foundation of China (Grant

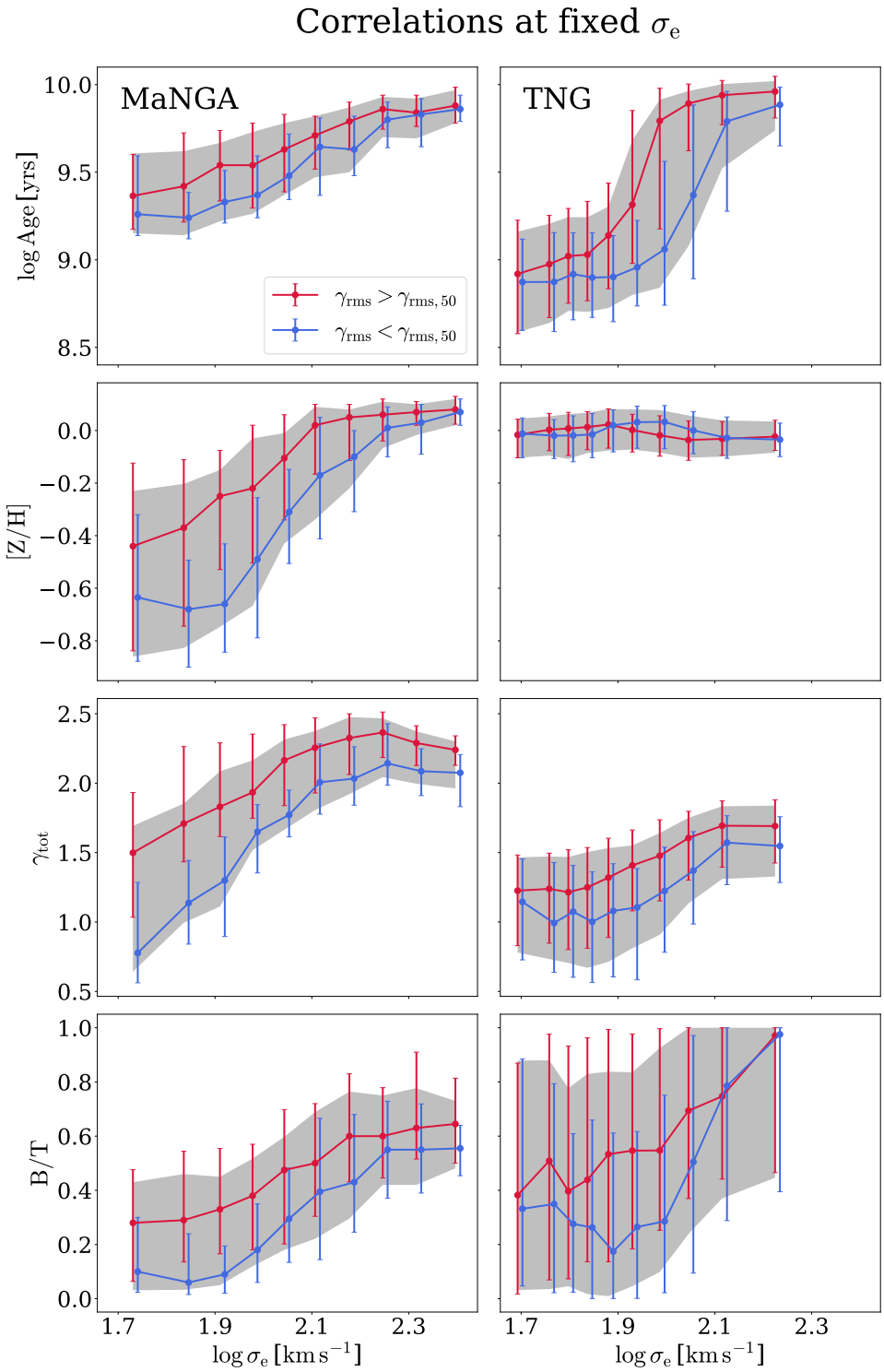


Figure 5. The trend of galaxy properties as a function of $\log \sigma_e$. Results of the stellar age, metallicity, the total density slope $\gamma_{\rm tot}$, and the bulge fraction B/T are shown from top to bottom. The left panels are for MaNGA galaxies and the right panels are for TNG galaxies. In each panel, galaxies in each $V_{\rm rms}$ bin are divided into two subgroups ($\gamma_{\rm rms} > \gamma_{\rm rms,50}$ and $\gamma_{\rm rms} < \gamma_{\rm rms,50}$, where $\gamma_{\rm rms,50}$ is the median value of $\gamma_{\rm rms}$ in each $V_{\rm rms}$ bin). Red and blue dots denote the median values of galaxy properties as shown in the Y-axis of the two subgroups ($\gamma_{\rm rms} > \gamma_{\rm rms,50}$ and $\gamma_{\rm rms} < \gamma_{\rm rms,50}$) with error bars indicating the range from the 16th to the 84th percentiles (1σ). The grey shaded region indicates the same 1σ range for the relations between galaxy properties and σ_e for all MaNGA (left panels) and TNG (right panels) galaxies.

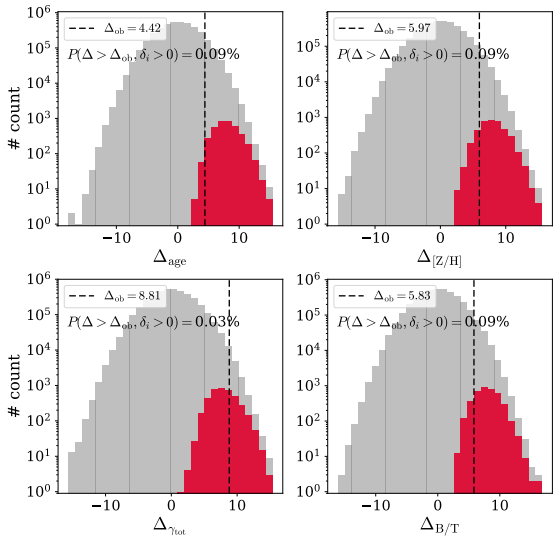


Figure 6. The distributions of sampled values for age (upper left), metallicity (upper right), $\gamma_{\rm tot}$ (bottom left), and B/T (bottom right). In each panel, the grey histograms indicate the distribution of sampled values, while the red histograms indicate the distribution of sampled values which satisfy the criterion of all sampled $\delta_i > 0$. The black dashed line indicates the $\Delta_{\rm ob}$ for age, metallicity, $\gamma_{\rm tot}$, and B/T. The probability $P(\Delta > \Delta_{\rm ob},\ \delta_i > 0)$ in each panel indicates the fraction of sampled values which satisfy both $\Delta > \Delta_{\rm ob}$ and all sampled $\delta_i > 0$.

Nos. 11821303, 11761131004 and 11761141012 to SM, 11903046 to JG), and by the Beijing Municipal Natural Science Foundation (No. 1204038 to JG). RL is supported by National Natural Science Foundation of China (Nos. 11773032 and 118513) and the NAOC Nebula Talents Program.

REFERENCES

Abolfathi B., et al., 2018, ApJS, 235, 42
Binney J., Tremaine S., 2008, Galactic Dynamics: Second Edition. Princeton University Press, Princeton, NJ
Bundy K., et al., 2015, ApJ, 798, 7
Cappellari M., 2002, MNRAS, 333, 400
Cappellari M., 2008, MNRAS, 390, 71
Cappellari M., 2016, ARA&A, 54, 597
Cappellari M., 2017, MNRAS, 466, 798
Cappellari M., Copin Y., 2003, MNRAS, 342, 345
Cappellari M., Emsellem E., 2004, PASP, 116, 138
Cappellari M., et al., 2006, MNRAS, 366, 1126
Cappellari M., et al., 2011, MNRAS, 416, 1680
Cappellari M., et al., 2013a, MNRAS, 432, 1709
Cappellari M., et al., 2013b, MNRAS, 432, 1862
Cleveland W. S., Devlin S. J., 1988, Journal of the American Statistical Association, 83, 596
Dolag K., Borgani S., Murante G., Springel V., 2009, MNRAS, 399, 497
Drory N., et al., 2015, AJ, 149, 77
Dutton A. A., Treu T., 2014, MNRAS, 438, 3594
Emsellem E., Monnet G., Bacon R., 1994, A&A, 285, 723
Falcón-Barroso J., Sánchez-Blázquez P., Vazdekis A., Ricciardelli E., Cardiel N., Cenarro A. J., Gorgas J., Peletier R. F., 2011, A&A, 532, A95
Freeman K. C., 1970, ApJ, 160, 811
Gerhard O. E., Binney J. J., 1996, MNRAS, 279, 993
Graves G. J., Faber S. M., Schiavon R. P., 2009, ApJ, 698, 1590
Law D. R., et al., 2015, AJ, 150, 19
Li H., et al., 2018, MNRAS, 476, 1765
Li R., et al., 2019, MNRAS, 490, 2124
Lu S., et al., 2020, MNRAS, 492, 5930
Magorrian J., et al., 1998, AJ, 115, 2285
Marinacci F., et al., 2018, MNRAS, 480, 5113
McDermid R. M., et al., 2015, MNRAS, 448, 3484
Naiman J. P., et al., 2018, MNRAS, 477, 1206
Nelson D., et al., 2018, MNRAS, 475, 624
Nelson D., et al., 2019, Computational Astrophysics and Cosmology, 6, 2
Pillepich A., et al., 2018, MNRAS, 475, 648
Poci A., Cappellari M., McDermid R. M., 2017, MNRAS, 467, 1397
Rybicki G. B., 1987, in de Zeeuw P. T., ed., IAU Symposium Vol. 127, Structure and Dynamics of Elliptical Galaxies. p. 397, doi:10.1007/978-94-009-3971-4_41
Salim S., et al., 2016, ApJS, 227, 2
Sánchez-Blázquez P., et al., 2006, MNRAS, 371, 703
Scott N., et al., 2017, MNRAS, 472, 2833
Sersic J. L., 1968, Atlas de Galaxias Australes
Simard L., Mendel J. T., Patton D. R., Ellison S. L., McConnachie A. W., 2011, ApJS, 196, 11
Smee S. A., et al., 2013, AJ, 146, 32
Springel V., White S. D. M., Tormen G., Kauffmann G., 2001, MNRAS, 328, 726
Springel V., et al., 2018, MNRAS, 475, 676
Stoughton C., et al., 2002, AJ, 123, 485
Wang Y., et al., 2019, MNRAS, 490, 5722
Wang Y., et al., 2020, MNRAS, 491, 5188
Westfall K. B., et al., 2019, AJ, 158, 231
Xu D., Springel V., Sluse D., Schneider P., Sonnenfeld A., Nelson D., Vogelsberger M., Hernquist L., 2017, MNRAS, 469, 1824
Xu D., et al., 2019, MNRAS, 489, 842
Yan R., et al., 2016a, AJ, 151, 8
Yan R., et al., 2016b, AJ, 152, 197
van den Bosch F. C., 1997, MNRAS, 287, 543